

An *Insight*-HXMT view of the mHz quasi-regular modulation phenomenon in the black hole X-ray binary 4U 1630–47

ZI-XU YANG,^{1,2} LIANG ZHANG,¹ YUE HUANG,¹ QINGCUI BU,³ ZHEN ZHANG,¹ HE-XIN LIU,^{1,2} WEI YU,^{1,2} PENG-JU WANG,^{1,2} Q. C. ZHAO,^{1,2} L. TAO,¹ JIN-LU QU,¹ SHU ZHANG,¹ SHUANG-NAN ZHANG,^{1,2} LIMING SONG,^{1,2} FANGJUN LU,^{1,2} XUELEI CAO,¹ LI CHEN,⁴ CE CAI,¹ ZHI CHANG,¹ TIANXIAN CHEN,¹ YONG CHEN,¹ YUPENG CHEN,¹ YIBAO CHEN,⁵ WEIWEI CUI,¹ GUOQIANG DING,⁶ YUANYUAN DU,¹ GUANHUA GAO,^{1,2} HE GAO,^{1,2} MINGYU GE,¹ YUDONG GU,¹ JU GUAN,¹ CHENGCHENG GUO,^{1,2} DAWEI HAN,¹ JIA HUO,¹ SHUMEI JIA,¹ WEICHUN JIANG,¹ JING JIN,¹ LINGDA KONG,^{1,2} BING LI,¹ GANG LI,¹ WEI LI,¹ XIAN LI,¹ XUFANG LI,¹ ZHENGWEI LI,¹ CHENGKUI LI,¹ LIN LIN,⁴ CONGZHAN LIU,¹ TIPEI LI,^{1,7,2} XIAOBO LI,¹ XIAOHUA LIANG,¹ JINYUAN LIAO,¹ HONGWEI LIU,¹ XIAOJING LIU,¹ XUEFENG LU,¹ QI LUO,^{1,2} TAO LUO,¹ BINYUAN MA,^{1,2} RUICAN MA,^{1,2} XIANG MA,¹ BIN MENG,¹ YI NANG,^{1,2} JIANYIN NIE,¹ GE OU,⁸ XIAOQIN REN,^{1,2} NA SAI,^{1,2} XINYING SONG,¹ LIANG SUN,¹ YING TAN,¹ YOU LI TUO,¹ CHEN WANG,^{9,2} WENSHUAI WANG,¹ LINGJUN WANG,¹ YUSA WANG,¹ JIESHUANG WANG,¹⁰ XIANGYANG WEN,¹ BOBING WU,¹ BAIYANG WU,^{1,2} MEI WU,¹ SHUO XIAO,^{1,2} YUPENG XU,^{1,2} SHAOLIN XIONG,^{1,2} SHENG YANG,¹ YANJI YANG,¹ QIBIN YI,^{1,11} QIANQING YIN,¹ YUAN YOU,^{1,2} BING ZHANG,¹² FAN ZHANG,¹ HONGMEI ZHANG,¹ JUAN ZHANG,¹ WANCHANG ZHANG,¹ WEI ZHANG,^{1,2} BINBIN ZHANG,¹³ PENG ZHANG,¹ YIFEI ZHANG,¹ YUANHANG ZHANG,^{1,2} HAISHENG ZHAO,¹ XIAOFAN ZHAO,^{1,2} SHIJI ZHENG,¹ AND DENGKE ZHOU^{1,2}

¹Key Laboratory for Particle Astrophysics, Institute of High Energy Physics, Chinese Academy of Sciences, 19B Yuquan Road, Beijing 100049, China

²University of Chinese Academy of Sciences, Chinese Academy of Sciences, Beijing 100049, China

³Institut für Astronomie und Astrophysik, Kepler Center for Astro and Particle Physics, Eberhard Karls Universität, Sand 1, D-72076 Tübingen, Germany

⁴Department of Astronomy, Beijing Normal University, Beijing 100088, China

⁵Department of Physics, Tsinghua University, Beijing 100084, China

⁶Xinjiang Astronomical Observatory, Chinese Academy of Sciences, 150, Science 1- Street, Urumqi, Xinjiang 830011, China

⁷Department of Astronomy, Tsinghua University, Beijing 100084, China

⁸Computing Division, Institute of High Energy Physics, Chinese Academy of Sciences, 19B Yuquan Road, Beijing 100049, China

⁹Key Laboratory of Space Astronomy and Technology, National Astronomical Observatories, Chinese Academy of Sciences, Beijing 100012, China

¹⁰Max-Planck-Institut für Kernphysik, Saupfercheckweg 1, D-69117 Heidelberg, Germany

¹¹School of Physics and Optoelectronics, Xiangtan University, Yuhu District, Xiangtan, Hunan, 411105, China

¹²Department of Physics and Astronomy, University of Nevada, Las Vegas, NV 89154, USA

¹³School of Astronomy and Space Science, Nanjing University, Nanjing 210023, China

(Received January 1, 2018; Revised January 7, 2018; Accepted July 29, 2022)

Submitted to ApJ

ABSTRACT

Here we report the spectral-timing results of the black hole X-ray binary 4U 1630–47 during its 2021 outburst using observations from the Hard X-ray Modulation Telescope (*Insight*-HXMT). Type-C quasi-periodic oscillations (QPOs) in ~ 1.6 – 4.2 Hz and quasi-regular modulation (QRM) near 60 mHz are detected during the outburst. The mHz QRM has a fractional rms of $\sim 10\%$ – 16% in the 8–35 keV energy band with a Q factor (frequency/width) of ~ 2 – 4 . Benefiting from the broad energy band of *Insight*-HXMT, we study the energy dependence of the ~ 60 mHz QRM in 1–100 keV for the first time. We find that the fractional rms of the mHz QRM increases with photon energy, while the time lags of the mHz QRM are soft and decrease with photon energy. Fast recurrence of the mHz QRM, in a timescale of less than one hour, has been observed during the outburst. During this period, the corresponding energy spectra moderately change when the source transitions from the QRM state to the non-QRM state. The QRM phenomena also shows a dependence with the accretion rate. We suggest that the QRM could be caused by an unknown accretion instability aroused from the corona.

Corresponding author: Zi-Xu Yang
yangzx@ihep.ac.cn

Corresponding author: Liang, Zhang
zhangliang@ihep.ac.cn

Corresponding author: Qingcui, Bu
bu@astro.uni-tuebingen.de

Keywords: Accretion, Astrophysical black holes, Low-mass x-ray binary stars, Stellar mass black holes

1. INTRODUCTION

Black hole X-ray binary 4U 1630–47 is a transient source characterized by its frequent outbursts (Choudhury et al. 2015). The first known outburst was recorded by Vela-5B in 1969 (Priedhorsky 1986). After that, the source goes into outbursts frequently with a typical period of 600–700 days (Jones et al. 1976; Priedhorsky 1986; Parmar et al. 1995). No dynamical mass measurement has been made for 4U 1630–47 because of the difficulties in identifying an optical or IR counterpart up to now. By scaling the correlation of the photon index of the hard spectral component with low-frequency quasi-periodic oscillations (LFQPOs) and mass accretion rate, Seifina et al. (2014) estimated that the black hole mass as $\sim 10 M_{\odot}$ and the inclination angle as ≤ 70 deg. A potential distance of 4.7–11.5 kpc was obtained by investigating the dust-scattering halo created by 4U 1630–47 (Kalemci et al. 2018). Liu et al. (2021) suggested a moderately high spin of $a_* = 0.817 \pm 0.014$ (90% confident level) by fitting the reflection spectra of *Insight*-HXMT during its 2020 outburst. This value is lower than what had been reported by King et al. (2014), in which they suggested an extreme high spin of $a_* = 0.985^{+0.005}_{-0.014}$ and an inclination angle of $i = 64^{+2}_{-3}$ deg by fitting the *NuSTAR* spectra.

Fast variability observed in the X-ray band of black hole transients allows us to investigate the properties of the innermost region of accretion flow (van der Klis 2006; Belloni & Stella 2014). Meanwhile, the spectral-timing analysis allows us to understand the underlying radiation process. The Fourier transform serves as a powerful tool to study the fast X-ray variability (Ingram & Motta 2019). LFQPOs with frequencies of 0.1–30 Hz are common in black hole X-ray binaries. Based on the shape of the power density spectrum (PDS), LFQPOs are divided into three types, namely, type-A, B and C QPOs (Casella et al. 2005). The property of LFQPOs is highly correlated with spectral states. Type-C QPOs usually appear in the low-hard state and hard-intermediate state, whereas type-B and type-A QPOs appear in the soft-intermediate state. Rapid transitions between different types of QPOs are sometimes observed during the hard-to-soft transition (Soleri et al. 2008; Motta et al. 2011; Sriram et al. 2013; Zhang et al. 2021). The physical origin of the LFQPOs is still under debate. It is suggested that a precessing hot inner flow/jet base can modulate the X-ray emission and produce the type-C QPO (Done et al. 2007; Ingram et al. 2009; Ingram & Done 2010, 2011; Kalamkar et al. 2016; Huang et al. 2018; Bu et al. 2021; Ma et al. 2021; Méndez et al. 2022). This is currently the most promising model for type-C QPO. No comprehensive models have been proposed for the type-B and type-A QPOs.

In addition to different types of QPOs, we have observed quasi-regular flares or dips with a relatively long period of ~ 10 –200 s in the light curves of a handful of black hole candidates, e.g., 4U 1630–47 (Trudolyubov et al. 2001), GRS 1915+015 (Morgan et al. 1997), GRO J1655–40 (Remillard et al. 1999), IGR J17091–3624 (Altamirano et al. 2011; Zhang et al. 2013, 2014), H 1743–322 (Altamirano & Strohmayer 2012). These variability patterns show in the PDS as a broad peak at several tens of mHz. Trudolyubov et al. (2001) named these signals as quasi-regular modulations (QRM). Taking GRS 1915+015 as an example, GRS 1915+015 is characterized by its complex X-ray variability which can be divided into 14 classes (Belloni et al. 2000; Klein-Wolt et al. 2002; Hannikainen et al. 2005). One of the most focused variability classes is the so-called " ρ " class (or "heartbeat" state). "Heartbeat" state is characterized by its regular flares which last 40–200 s (Weng et al. 2018). During the flare period, hardness ratio between different energy bands shows complex signatures (Nielsen et al. 2012). Based on a phase-resolved study, Nielsen et al. (2012) found that the temperature at the inner edge of the accretion disk increases with flux while the inner radius of the disk decreases during the flares. All these results support a radiation-pressure-driven evaporation or ejection event occurred in the inner accretion disk. At the inner region of the accretion disk where radiation pressure dominates, limit-cycle behaviour of accretion disk will cause periodic flux modulation due to the thermal viscous instability when the mass accretion rate increases to a certain level (Lightman & Eardley 1974). The instability is usually used to explain the accretion rate dependent flux modulation. Based on a systematic analysis of the "heartbeat" state in GRS 1915+105, Weng et al. (2018) found tight correlations among the recurrence time, the inner radius of the disk, and the luminosity of the non-thermal emission. They suggested that the change of the corona size can result in the observed correlations.

Dieters et al. (2000) and Trudolyubov et al. (2001) studied the *RXTE* observations of 4U 1630–47 during its 1998 outburst. They found that during a certain plateau state ($\sim 1.4 \times 10^{-8}$ erg s $^{-1}$ cm $^{-2}$, 3–20 keV energy range), the source exhibits quasi-regular oscillations with a period of ~ 10 –20 s with simultaneous complex type-C QPOs. Trudolyubov et al. (2001) interpreted the type-C QPO by considering resonance oscillations of the shock, while the QRM is related to the time of the matter accumulation at the shock front (the shock stability timescale).

In 2021, 4U 1630–47 experienced an outburst (peak ~ 500 mCrab) after ~ 600 days from its 2020 outburst. In this work, we report the detection of the mHz QRM phenomenon dur-

ing this outburst, and present a detailed study of the mHz QRM from 4U 1630–47, in which we have extended its energy dependence study up to 60–100 keV for the first time. In addition, we compare the spectra of the periods with different types of PDS to unveil the spectral parameters that are responsible for the transition. In Section 2, we describe the observation and data reduction process. The data analysis and results are presented in Section 3. We discuss our results in Section 4.

2. OBSERVATIONS AND DATA REDUCTION

Insight-HXMT is China’s first X-ray astronomy satellite, launched on 2017 June 15 (Zhang et al. 2020). It carries three slat-collimated instruments: the High Energy X-ray

telescope (HE: 20–250 keV, Liu et al. 2020), the Medium Energy X-ray telescope (ME: 5–30 keV, Cao et al. 2020), and the Low Energy X-ray telescope (LE: 1–15 keV, Chen et al. 2020). Each telescope carries both large and small field-of-view (FoV) detectors in order to facilitate the background analyses. The small FoV detectors (LE: $1^\circ.6 \times 6^\circ$; ME: $1^\circ \times 4^\circ$; HE: $1^\circ.1 \times 5^\circ.7$) have a lower probability of source contamination, and thus are more suitable for pointing observation¹. *Insight*-HXMT started a high cadence monitoring of 4U 1630–47 from 2021 September 18 to 28 (see Table 1 for the log of the *Insight*-HXMT observation). The *Insight*-HXMT observations stopped after 2021 September 28 due to the small solar aspect angle ($< 70^\circ$).

Table 1. *Insight*-HXMT observations of 4U 1630–47 in the 2021 outburst.

ObsID	Start Time (MJD)	LE Rate (cts s ⁻¹)	ME Rate (cts s ⁻¹)	HE Rate (cts s ⁻¹)	PDS ^a	Centroid Frequency (Hz)	Fractional rms ^b (%)	Q factor ^c
P040426300101	59475.647	5.2 ± 0.1	32.8 ± 0.2	74.5 ± 0.2	QPO	1.68 ^{+0.02} _{-0.03}	20.63 ^{+1.58} _{-3.73}	4.88 ^{+1.24} _{-1.94}
P040426300201	59476.488	7.6 ± 0.1	36.7 ± 0.1	93.8 ± 0.1	QPO	2.43 ^{+0.01} _{-0.01}	18.20 ^{+0.74} _{-0.74}	9.33 ^{+1.35} _{-1.14}
P040426300301	59477.647	10.3 ± 0.2	36.0 ± 0.2	92.9 ± 0.2	QPO	2.88 ^{+0.02} _{-0.02}	16.82 ^{+1.70} _{-1.41}	11.54 ^{+5.04} _{-3.32}
P040426300401	59478.906	13.9 ± 0.1	39.9 ± 0.1	93.5 ± 0.2	QPO	3.55 ^{+0.04} _{-0.04}	16.18 ^{+1.06} _{-1.06}	6.83 ^{+1.55} _{-1.21}
P040426300501	59479.647	25.4 ± 0.3	64.7 ± 0.2	125.7 ± 0.3	QPO	4.28 ^{+0.16} _{-0.23}	7.70 ^{+1.94} _{-2.05}	6.48 ^{+6.29} _{-5.29}
P040426300601	59480.641	28.0 ± 0.3	61.6 ± 0.2	120.0 ± 0.3	QPO	4.17 ^{+0.05} _{-0.05}	8.17 ^{+1.31} _{-1.20}	16.68 ^{+10.49} _{-6.81}
P040426300701	59481.667	10.0 ± 0.2	34.7 ± 0.2	80.4 ± 0.3	QPO	2.35 ^{+0.05} _{-0.06}	15.80 ^{+2.09} _{-2.43}	9.02 ^{+3.46} _{-4.14}
P040426300801	59482.626	13.7 ± 0.1	40.2 ± 0.2	80.5 ± 0.2	QPO	3.32 ^{+0.07} _{-0.08}	18.92 ^{+1.95} _{-1.78}	3.68 ^{+1.33} _{-0.97}
P040426300901	59483.785	48.6 ± 0.3	112.5 ± 0.3	192.0 ± 0.9	QRM	0.062 ^{+0.001} _{-0.001}	12.53 ^{+0.72} _{-0.72}	2.96 ^{+0.80} _{-0.49}
P040426300902	59483.888	48.2 ± 0.3	106.9 ± 0.2	159.8 ± 0.2	QRM	0.064 ^{+0.001} _{-0.001}	14.32 ^{+0.68} _{-0.68}	3.51 ^{+0.71} _{-0.46}
P040426300903	59484.022	48.4 ± 0.2	109.4 ± 0.3	175.5 ± 0.4	QRM	0.060 ^{+0.002} _{-0.002}	12.04 ^{+0.57} _{-0.57}	1.90 ^{+0.55} _{-0.28}
P040426301001	59484.932	55.2 ± 0.3	114.3 ± 0.2	163.7 ± 0.3	QRM	0.053 ^{+0.001} _{-0.001}	14.41 ^{+0.62} _{-0.62}	2.04 ^{+0.47} _{-0.29}
P040426301002	59485.050	53.4 ± 0.4	115.5 ± 0.3	181.0 ± 1.4	QRM	0.059 ^{+0.001} _{-0.001}	10.98 ^{+1.26} _{-1.26}	8.36 ^{+4.46} _{-3.86}
P040426301003	59485.240	67.9 ± 0.3	131.1 ± 0.2	160.2 ± 0.2	None/QRM	0.055 ^{+0.001} _{-0.002}	16.54 ^{+1.05} _{-1.05}	3.40 ^{+0.90} _{-0.57}
P040426301004	59485.373	75.0 ± 0.3	149.8 ± 0.3	166.1 ± 0.2	None	None	None	None
P040426301005	59485.506	80.7 ± 0.3	154.3 ± 0.3	181.2 ± 0.3	None	None	None	None
P040426301006	59485.639	80.1 ± 0.3	148.5 ± 0.4	165.8 ± 0.5	None	None	None	None
P040426301007	59485.771	78.4 ± 0.3	149.9 ± 0.3	172.4 ± 0.5	None	None	None	None
P040426301008	59485.909	79.1 ± 0.3	152.0 ± 0.2	167.3 ± 0.2	None	None	None	None

^aThe properties of the QPO and QRM are measured from the PDS of ME 8–35 keV.

^bThe fractional rms is measured for the QPO/QRM component.

^cThe quality factor Q is defined as centroid frequency/FWHM.

The data are extracted from all three instruments using the *Insight*-HXMT Data Analysis software (HXMTDAS) v2.05

¹ <http://hxmtcn.ihep.ac.cn/AboutHxmt.jhtml>

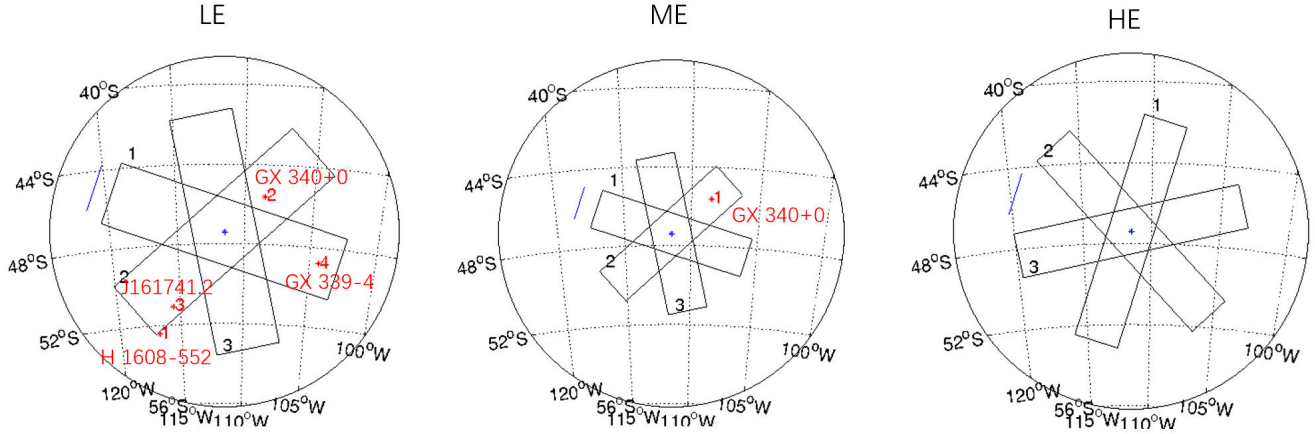


Figure 1. The small FoVs of LE (left), ME (middle) and HE (right). The locations and names of the contamination sources during our observations are marked with red.

², and filtered with the following criteria: (1) pointing offset angle less than 0.04° ; (2) Earth elevation angle larger than 10° ; (3) the value of the geomagnetic cutoff rigidity larger than 8 GV; (4) at least 300 s before and after the South Atlantic Anomaly passage. To avoid possible contamination from the bright Earth and nearby sources, we only use data from the small field of view (FoV) (Chen et al. 2018). The energy bands adopted for spectral analysis are 2–8 keV for LE, 8–28 keV for ME, and 28–100 keV for HE.

2.1. Background

The background estimations of LE, ME, and HE are performed using the stand-alone Python scripts LEBKGMAP, MEBKGMAP, and HEBKGMAP (Liao et al. 2020a,b; Guo et al. 2020). 4U 1630–47 locates in a crowded region near the Galactic plane. As a result, it may be contaminated by some other bright X-ray sources (Kuulkers et al. 1997). In Figure 1, we show the small FoVs of LE, ME, and HE, respectively. Each instrument consists of three Detection Boxes (DetBox No. 1, 2, and 3). As can be seen, relatively bright contaminating sources in the small FoVs of 4U 1630–47 are GX 340+0, GX 339–4, H1608–552 and J161741.2–510455. H1608–552 and J161741.2–510455 are transient sources that were in a quiescence state during the outburst of 4U 1630–47, thus their contribution can be ignored. GX 340+0 is a persistent Z source that shows fast X-ray variability. It constantly appears in the No.2 DetBox of the LE detector and No.2 DetBox of the ME detector. Following Bu et al. (2021), We create light curves and spectra from each DetBox and find that the contribution of the X-ray flux from GX 340+0 is larger than 5% for the LE and ME detectors. In addition, GX 339–4 was at the

end stage of the outburst in 2021. It constantly appears in the No.1 DetBox of the LE detector, and contributes more than 50% extra counts to the LE No.1 DetBox detector. Therefore, we do not use the data from the No.1 and 2 DetBox of the LE detector and the No.2 DetBox of the ME detector for the following timing and spectral analysis.

3. ANALYSIS AND RESULTS

3.1. Fundamental diagrams

In the upper panel of Figure 2, we show the 2–20 keV light curve of 4U 1630–47 from its 2021 outburst obtained with MAXI/GSC. Three peaks can be observed from the light curve. The *Insight*-HXMT observations were performed during the initial rising phase of the first main peak. In the lower panel of Figure 2, we show the hardness-intensity diagram (HID) of this outburst. Based on their locations in the HID, we can identify that our *Insight*-HXMT observations are made during the intermediate state. In the 2021 outburst although we still lack bright hard states as previous outbursts (Abe et al. 2005; Tomsick et al. 2014; Capitanio et al. 2015), *Insight*-HXMT accumulates intensive observations in hard-intermediate/steep power-law state which are rare during *RXTE* epochs (Tomsick et al. 2005; Connors et al. 2021).

In Figure 3, we show the *Insight*-HXMT LE (1–10 keV), ME (8–35 keV), and HE (30–150 keV) light curves, together with the 0.01–64 Hz fractional rms, calculated in the ME (8–35 keV) band, and the hardness ratio, defined as the ratio of the count rates between the ME 20–30 keV and ME 10–20 keV bands, evolution during the outbursts. The LE/ME/HE count rates slowly increase from initial value, jump to a plateau around MJD 59483, and then remain stable at this flux level for about 3 days. Afterwards, the count rates rapidly increase to a higher flux level, accompanied by a decrease in hardness

² The data analysis software is available from <http://hxmten.ihep.ac.cn/software.jhtml>.

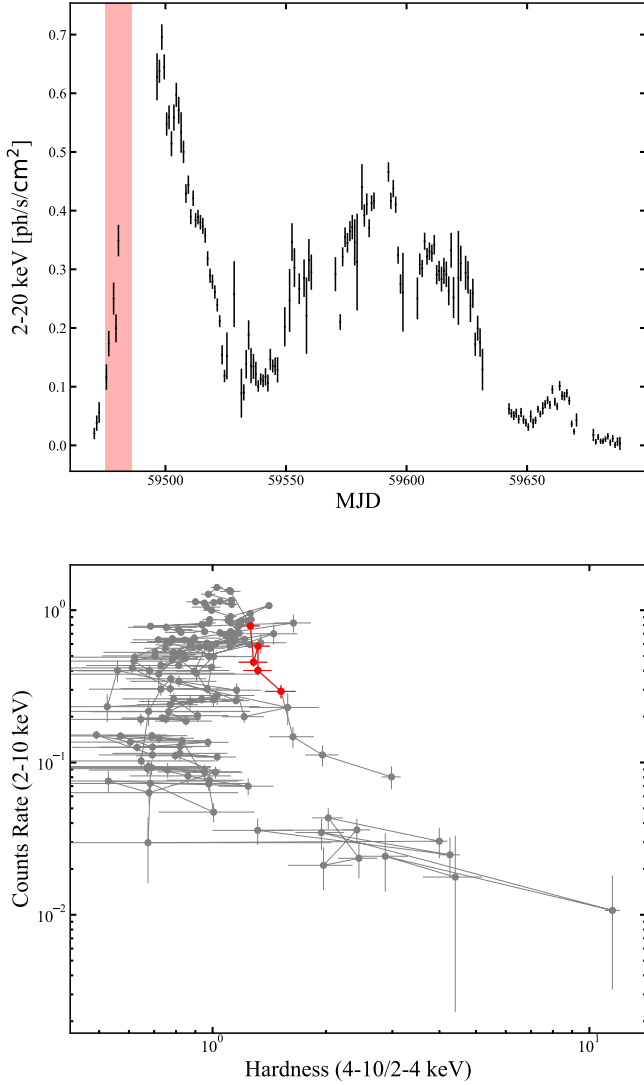


Figure 2. *Upper panel:* The 2–20 keV light curve of 4U 1630–47 in its 2021 outburst obtained with MAXI/GSC. The red region marks the time interval with *Insight*-HXMT observations (MJD 59475–59486). *Bottom panel:* the hardness-intensity diagram of 4U 1630–47 in its 2021 outburst obtained with MAXI/GSC. The red points highlight the observations located in the red region of the upper panel.

ratio. Meanwhile, at the beginning of the observation, the total fractional rms remains above 20%, whereas after MJD 59483, the rms drops sharply to between 20% and 10%. After MJD 59485, the PDS shows a very low rms amplitude (<5%).

3.2. Timing analysis

To study the fast X-ray variability, we create an averaged power spectrum for each of the *Insight*-HXMT observations. Based on the characteristics of the light curves and PDS, we divide the X-ray variability into three different types. In Figure 4, we show the representative light curves and their corresponding PDS for the three types, respectively. Dur-

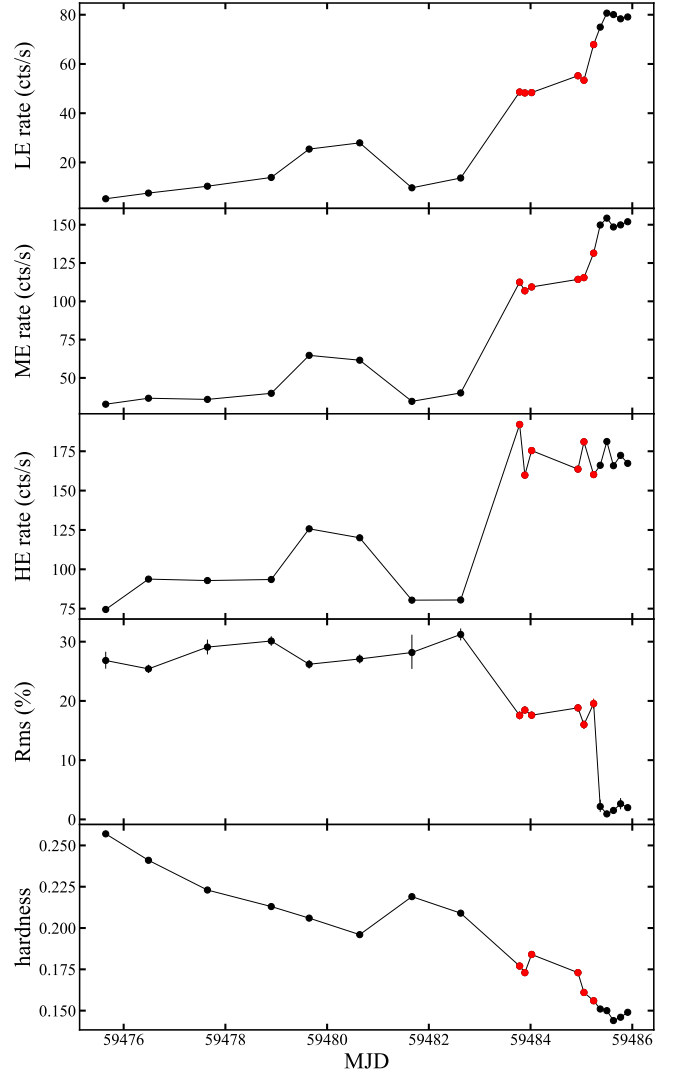


Figure 3. *Insight*-HXMT LE (1–10 keV), ME (8–35 keV), and HE (30–150 keV) light curves, together with the 0.01–64 Hz fractional rms, calculated in the 8–35 keV (ME) band, and the hardness ratio defined as the ratio of the count rates between the ME 20–30 keV and ME 10–20 keV bands. The red points mark the observations with the mHz QRM.

ing MJD 59475.6–59482.6, the PDS (the left panels of Figure 4) is characterized by a relatively narrow QPO centered at 1.6–4.2 Hz with a band-limited noise component at low frequencies. During MJD 59483.8–59485.2, the PDS (the middle panels of Figure 4) is characterized by a relatively broad peak ($Q \sim 2 - 4$) near 60 mHz accompanied with a broadband noise component above its frequency. The corresponding light curves show regular flares of ~ 16 s, which are clearly different from the light curves of the first type. We further refer this regular modulated signal as mHz QRM to distinguish it from the first type. In addition, the mHz QRM shows a transient behaviour near MJD 59485: the mHz QRM disappears in the first two orbits of this observation (ObsID

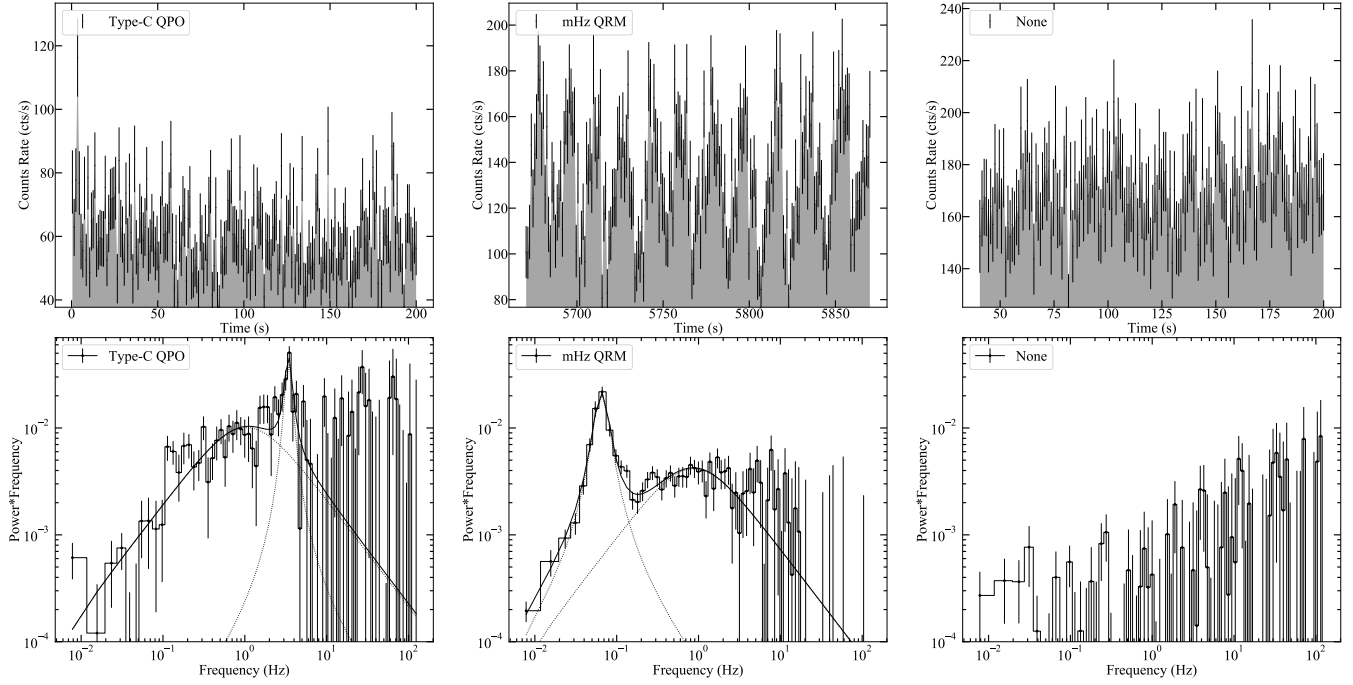


Figure 4. Representative light curves (ME 8–35 keV) and the corresponding power density spectra for different classes of X-ray variability observed in 4U 1630–47 with *Insight*-HXMT. *Left panel:* the light curve and PDS with a typical type-C QPO. *Middle panel:* the light curve and PDS with a mHz QRM. *Right panel:* the light curve and PDS when no QPO/QRM is observed.

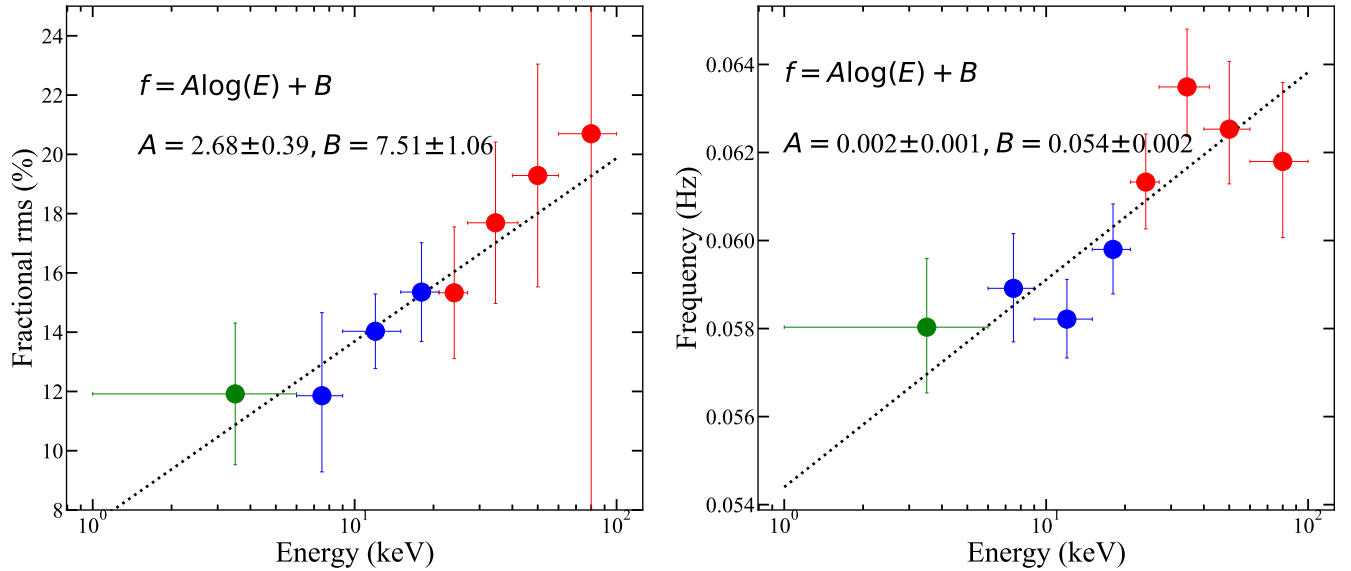


Figure 5. Fractional rms (left) and characteristic frequency (right) of the mHz QRM as a function of photon energy. The green, blue, red points represent the LE, ME and HE data, respectively. The dotted line represents the best-fitted line with a function of $f = A * \log(E) + B$. The fractional rms and characteristic frequency are measured from the PDS averaged from all the observations with the mHz QRM (ObsIDs P040426300901, P040426300902, P040426300903, P040426301001, P040426301002, P040426301003).

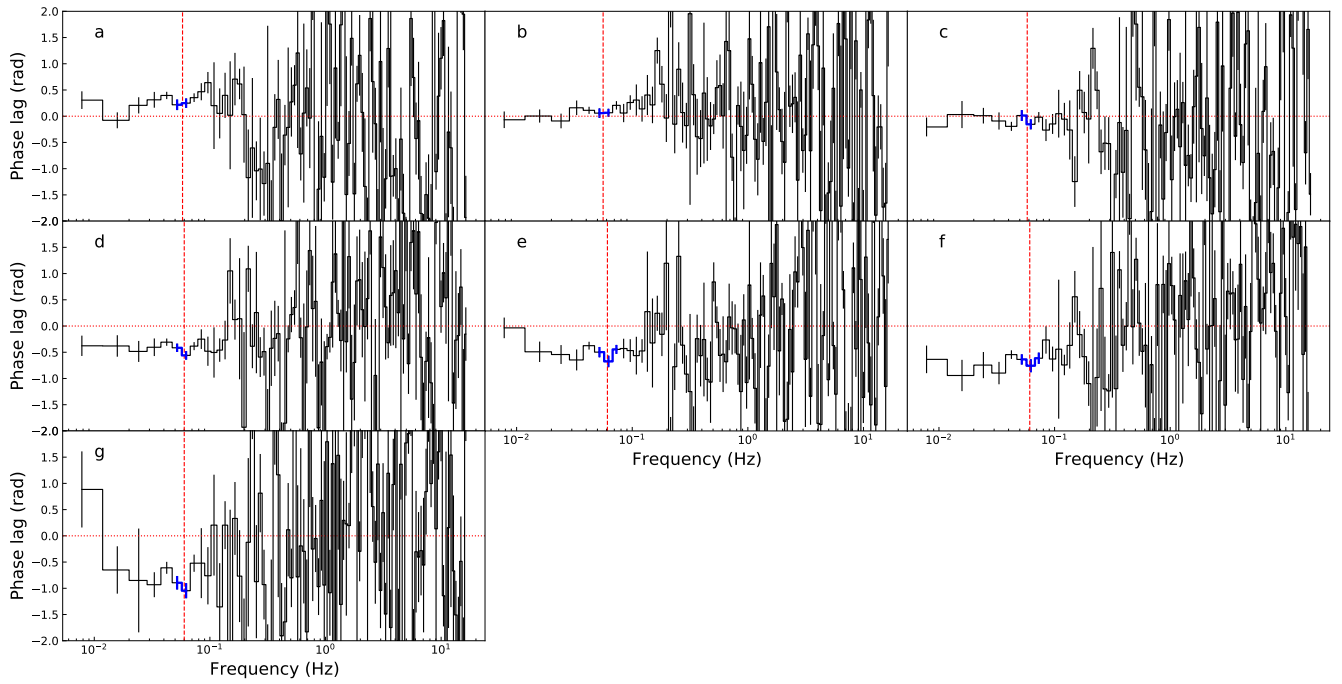


Figure 6. Frequency-dependent phase-lag spectra in different energy bands for the observations with the mHz QRM. The reference energy band is LE 1–6 keV. The chosen energy bands are 6–9 keV (a), 9–15 keV (b), 15–21 keV (c), 21–27 keV (d), 27–40 keV (e), 40–60 keV (f), and 60–100 keV (g). The red vertical line marks the centroid frequency of the mHz QRM. The blue points mark the frequency range ($\nu_0 - \text{FWHM}/2$, $\nu_0 + \text{FWHM}/2$) over which the phase-lags of the mHz QRM are averaged. Same as Figure 5, the data we used are from all the observations with the mHz QRM.

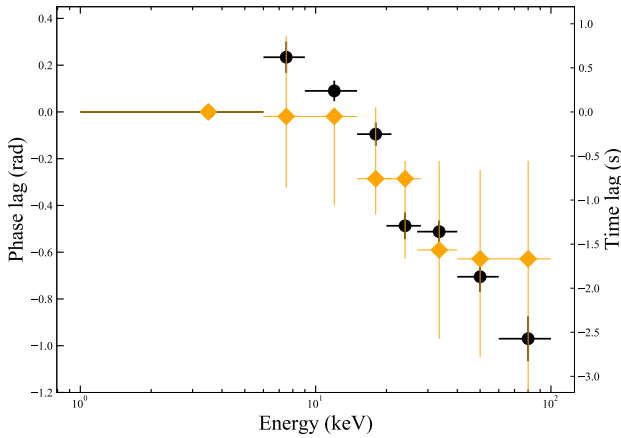


Figure 7. Phase/time lags as a function of photon energy. The reference energy band is LE 1–6 keV. The chosen energy bands are 6–9 keV, 9–15 keV, 15–21 keV, 21–27 keV, 27–40 keV, 40–60 keV, and 60–100 keV. The black points are the phase/time lags of the mHz QRM measured from the frequency-dependent phase-lag spectra by averaging the lags in the QRM frequency range ($\nu_0 \pm \text{FWHM}/2$, blue points in Figure 6). The orange points are the time lags measured from cross-correlation in time domain of two different energy band light curves.

P040426301003) and appears again in the last two orbits. After MJD 59485.4, the PDS is dominated by Poisson noise without QPO/QRM.

For further studies, we create PDS with a 128 s long interval and 1/256 s time resolution. The PDS is applied to Miyamoto normalization (Miyamoto et al. 1991). We then fit the PDS with a multiple-Lorentzian model (Belloni et al. 2002) (see Figure 4). From the fittings, we obtain the fractional rms and characteristic frequency of the QPO/QRM. The fractional rms is background corrected according to the formula: $rms = \sqrt{P} \times (S+B) / S$ (Belloni & Hasinger 1990; Bu et al. 2015). The maximum power is observed at the characteristic frequency $\nu_{\max} = \sqrt{\nu_0^2 + (\sigma/2)^2}$, where ν_0 is the centroid frequency and σ is the FWHM of the Lorentzian function (Belloni et al. 1997b). The values of the frequency and rms of the QPO/QRM are listed in Table 1.

Two Lorentzian components are required to fit the PDS of the 1.6–4.2 Hz QPO: a narrow peak and a low-frequency broadband noise component. The frequency of the QPO is anti-correlated with spectral hardness and QPO fractional rms. The Q factor of this QPO is in the range of ~ 4 –10, with a fractional rms amplitude of ~ 8 –21%. The broadband noise component is relatively strong with a typical rms of 20%. Based on these characteristics, we identify this QPO as the type-C QPO detected in black hole X-ray binaries.

The PDS of the mHz QRM can be well fitted with two Lorentzian functions. However, their properties are quite

different from those of the 1.6–4.2 Hz QPOs. The frequency of the peak is around 0.06 Hz, and stays stable among different observations. The width of the peak is broad, with a Q factor of ~ 2 –4. The fractional rms amplitude of the mHz peak is ~ 11 –16%. The broadband noise component above the 0.06 Hz peak has a relatively lower rms of ~ 10 %. From the view of the light curves, the mHz flux modulation is characterized by a fast rise following by a fast decay. The rise and decay times of the flare are almost the same (~ 8 s). This is different from the characteristics of the "heartbeat" light curves, which typically show a slow rise and fast decay profile (Weng et al. 2018; Mineo et al. 2021).

We further study the energy-dependent properties of the mHz QRM. Since the properties of the mHz QRM are similar among observations, we combine all the observations with the mHz QRM detection and compute averaged PDS for different energy bands. The fractional rms and the characteristic frequency of the mHz QRM as a function of photon energy are shown in Figure 5. From the left panel of Figure 5, we can see a positive correlation between the fractional rms of the mHz QRM and photon energy in the 1–100 keV energy band. The value of the rms increases from $\sim 12\%$ to $\sim 20\%$. In order to check the significance of the increase, we fit this relation with a function of $f = A * \log(E) + B$. The best-fitting slope is $A = 2.68 \pm 0.39$, which is more than 6σ from zero. There is also a slightly increasing trend in characteristic frequency (the right panel of Figure 5). However, the change in characteristic frequency is relatively small, from $0.058^{+0.002}_{-0.001}$ Hz to $0.064^{+0.001}_{-0.001}$ Hz. We fit this relation with the function $f = A * \log(E) + B$. The best-fitting slope $A = 0.002 \pm 0.001$ is consistent with being zero within $\sim 2\sigma$ level, suggesting that there is no significant change in characteristic frequency. Meanwhile, it should be noted that the mHz QRM peak is broad, and its rms or frequency could be affected by the variation of the underlying broad band noise component. In particular, a strong energy dependence of the broad band noise component has been found in previous studies (Yang et al. 2022; Feng et al. 2022).

Phase/time lag is a commonly used tool to study the X-ray variability and can help us understand the geometry of the emission area. In Figure 6, we show the frequency-dependent phase-lag spectra for different energy bands, relative to the same reference band 1–6 keV. From this figure, we do not see clear features around the mHz QRM frequency range. The phase lags below 0.1 Hz remain more or less constant. This is consistent with the fact that the PDS below 0.1 Hz is completely dominated by the Lorentzian component of the QRM. This is in sharp contrast with that type-C QPOs, which are strongly interfered by the underlying broadband noise (Ma et al. 2021). Above 0.1 Hz, the phase lags can not be constrained well. We calculate the phase lags of the mHz QRM by averaging the lags over the mHz QRM frequency

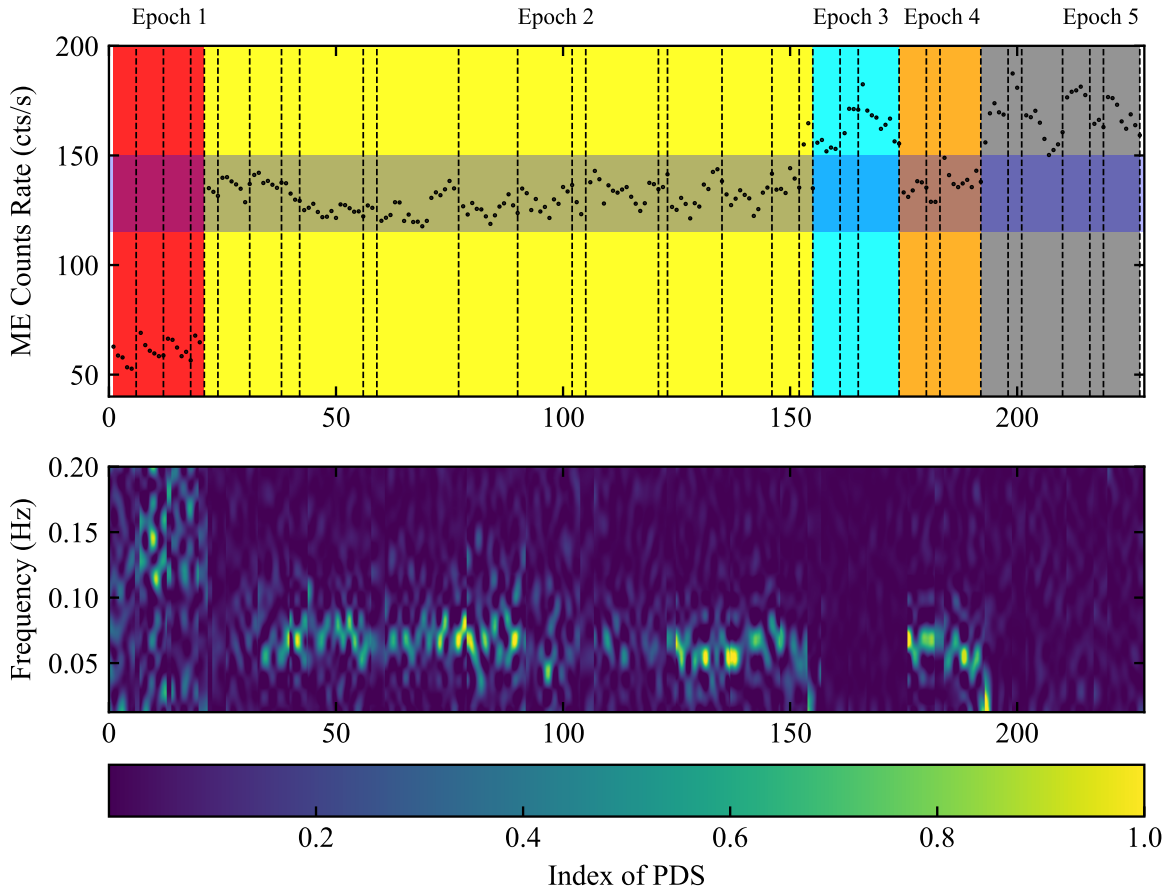


Figure 8. ME 8–35 keV light curve and the corresponding dynamical PDS for a particular period that shows fast transitions among different kinds of PDS. The bin size of the light curve is 80 s. In the top panel, the dashed lines mark the time gaps between orbits. In the bottom panel, the x -axis represents the index of each PDS. We divide this period into five epochs: epoch 1 (P040426300801), the period with a type-C QPO in the PDS; epoch 2 (P040426300901, P040426301001, P040426301002), the period shows a mHz QRM; epoch3 (the first part of P040426301003), the period when mHz QRM disappears and the PDS is dominated by Poission noise; epoch 4 (the last part of P040426301003), the period when the mHz QRM reappears, and epoch 5 (ObsID P040426301004) where QRM disappears again.

range $\nu_0 \pm \text{FWHM}/2$, as we commonly do for QPOs (Vaughan & Nowak 1997; Qu et al. 2010; Zhang et al. 2017). The results are shown in Figure 7 with black points. Below 10 keV, we find a slight hard lag or zero lag. Above 10 keV, the lags are soft and decrease with energy up to 100 keV. Since the light curve is mainly dominated by the flare (QRM), we also calculate the time lags from the cross-correlation in time domain (see orange points in Figure 7). Although the errors of the time lags measured from the cross-correlation are very large, we can see that the trend of the black and orange points is consistent.

3.3. Spectral changes during the transitions between different kinds of PDS

During the period between MJD 58482–58485, we observe fast transitions among different types of PDS, as shown in

Figure 4. In Figure 8, we show the ME 8.0–35.0 keV light curve with 80-s binning and the corresponding dynamical PDS within this period. The dashed lines in the top panel mark the time gaps between orbits. The x -axis label is the index of each 80-s PDS. Based on the characteristic of the PDS and the flux level, we divide this period into 5 epochs. During epoch 1, significant type-C QPOs with a strong band-limited noise at low frequencies are observed in the PDS. The type-C QPO disappears in epoch 2 and is replaced by the mHz QRM. The mHz QRM disappears in epoch 3, re-appears in epoch 4, and then disappears in epoch 5. It is clear that the mHz QRM is only observed within a narrow flux range (ME 8–35 keV count rates $\sim 120 - 150 \text{ cts s}^{-1}$). The behaviour of the regular flux modulation disappears outside of this range.

To study the spectral changes during the transitions among the epochs, we extract background-subtracted spectra for

the 5 epochs, separately. We use XSPEC v12.12.0 for the following spectral studies (Arnaud 1996). We have tried several continuum models, and found that the model `constant*TBabs*thcomp*diskbb` is the best-fitting model. In this model, the multiplicative constant is used to quantify the cross-calibration uncertainties between the three instruments of *Insight*-HXMT. The component `thcomp` is a novel thermal Comptonization convolution model to describe the broadband X-ray power-law continuum, which is presented as a replacement for the `nthcomp` model (Zdziarski et al. 1996, 2020; Dziełak et al. 2021; Wang et al. 2022). To use the `thcomp` convolution model, we extend the energy grid from 0.1 keV to 500 keV with the XSPEC command `ENERGIES` to treat with the limited response matrices at high or low energies. Because the distance of 4U 1630–47 is not precisely measured, the hydrogen column density is still not well determined ($N_{\text{H}} = (5 - 12) \times 10^{22} \text{ cm}^{-2}$) (Tomsick et al. 1998; Pahari et al. 2018). Given that the column density of the Galactic absorption is not expected to change on short timescales, we fit the five spectra simultaneously with N_{H} linked.

The best-fitting spectral parameters are listed in Table 2. The errors are given at 1σ level. The best-fitting models are shown in Figure 9, along with the residual of each spectrum. From our fits, we get a moderate value of $N_{\text{H}} = 8.24^{+0.03}_{-0.07} \times 10^{22} \text{ cm}^{-2}$, which is consistent with previous results (Trudolyubov et al. 2001; Baby et al. 2020).

We first compare the spectra of the period with the type-C QPO and that with the mHz QRM (epochs 1 and 2). From epoch 1 to epoch 2, the disk temperature increases from $1.02^{+0.10}_{-0.10}$ keV to $1.16^{+0.02}_{-0.02}$ keV, accompanied by an increase in `diskbb` normalization. In addition to the disk variation, the electron temperature kT_e increases slightly from $20.7^{+2.8}_{-2.0}$ keV to $29.5^{+1.4}_{-1.3}$ keV. Meanwhile, a smaller optical depth is seen in epoch 2 ($\tau_{\text{hot}} = 1.84^{+0.07}_{-0.07}$) than that in epoch 1 ($\tau_{\text{hot}} = 2.93^{+0.27}_{-0.35}$).

We then compare the spectra of the period with and without the mHz QRM (epochs 2, 3, 4 and 5). The disk temperature is lower when the QRM appears, while the `diskbb` normalization is slightly higher. The optical depth of the Comptonization region is slightly higher when the QRM appears.

Apart from the differences discussed above, f_{sc} is constrained at its upper limit for epochs 2,3,4 and 5, but its value is slightly smaller in epoch 1.

In order to constrain the minimum set of spectral parameters that dominate the spectral changes, we conduct a simultaneous fit for two sets of spectra: the spectra of the epochs with the type-C QPO and the QRM (epochs 1 and 2), and the spectra of the epochs with and without the QRM (epochs 2 and 3). As Sriram et al. (2013) did for type-B QPO, we first tie all parameters together, which leads to a very high $\chi^2/d.o.f.$. We then untie the parameters of `diskbb` and `thcomp` one by

one, and check the change of $\chi^2/d.o.f.$ (see Table 3). We find that, for both sets of spectra, untying the parameters of the disk component significantly improves the fits. The two parameters of `diskbb`, T_{in} and $norm$, are highly correlated. Therefore, it is hard to distinguish which parameter leads to the changes. Freeing T_{in} only or freeing $norm$ only results in a similar $\chi^2/d.o.f.$. For both sets of spectra, the optical depth of the corona is also needed to be free to obtain an acceptable fit. Allowing kT_e and f_{sc} to vary only marginally improves the fit for the set epochs 1 and 2, and does not improve the fit any more for the set epochs 2 and 3. We have also tried to free the `thcomp` parameters first. However, freeing all the parameters of `thcomp` still leads to an unacceptable fit with $\chi^2/d.o.f. \gtrsim 2$.

Moreover, due to the relatively low flux of the source at the time of observation, we cannot perform phase-resolved spectral study or time-resolved spectral study for 4U 1630–47 as done for GRS 1915+105 (Nielsen et al. 2012; Rawat et al. 2022). Nevertheless, we performed a simple flux-resolved spectra comparison for the mHz QRM. We extracted spectra from data above the average count rate and below the average count rate, respectively. We fit the low-flux and high-flux spectra jointly with the model `constant * TBabs * thcomp * diskbb`. The results show a slight difference in normalization, while the other parameters remain consistent within 1σ error.

4. DISCUSSION

In section 3, we have carried out a detailed timing and spectral analysis of the five epochs with type-C QPO and the secular mHz QRM in 4U1630-47, as observed by *Insight*-HXMT during the 2021 outburst. In this section, we will discuss the possible mechanisms behind the mHz QRM based on above results.

4.1. Appearance of the mHz QRM

In terms of 2021 outburst, the mHz QRM appears shortly after the disappearance of type-C QPO within one day (from MJD 59482.626 to MJD 59483.785), along with a drop of total fractional rms (see Figure 3). In the bottom panel of Figure 3, the fractional rms remains stable before MJD 59483 when the type-C QPO is prominent in PDS. After MJD 59483, the rms amplitude decreases from above 25% to below 20% when the mHz QRM appears. The drop of fractional rms during intermediate state is usually accompanied by the transition from hard intermediate state to soft intermediate state.

A similar mHz QRM was also observed in the 1998 outburst of 4U 1630–47 with *RXTE* (Trudolyubov et al. 2001). However, the light curves of the mHz QRM seen in the 1998 and 2021 outbursts are quite different. For the mHz QRM in the 1998 outburst, the light curve is characterized by the presence of quasi-regular dips with a period of ~ 10 – 20 s,

Table 2. Spectral parameters of all epochs using the model `constant * TBabs * thcomp * diskbb`. N_{H} is the X-ray absorption column density. T_{in} is the temperature at inner disk radius. Norm is the normalization parameter of `diskbb`. τ_{hot} is the Thomson optical depth. kT_{e} is the electron temperature. f_{sc} is the scattering fraction. R_{in} is the apparent disk radius, defined as $R_{\text{in}} = \sqrt{\text{norm}/\cos\theta} \times D_{10}$, where D_{10} is the source distance in units of 10 kpc and θ is the inclination angle of the accretion disk. Here we adopt $D_{10} = 1$ and $\theta = 64^\circ$ (King et al. 2014). The letter F indicates that the parameter was fixed. The letter P indicates that the error of the parameter pegged at the upper boundary.

Component	Parameter	Epoch 1	Epoch 2	Epoch 3	Epoch 4	Epoch 5
	constant (LE)	1.00 (F)	1.00 (F)	1.00 (F)	1.00 (F)	1.00 (F)
	constant (ME)	1.07	1.00	0.91	0.97	1.05
	constant (HE)	1.02	0.94	0.87	0.95	0.98
TBabs	$N_{\text{H}} (\times 10^{22} \text{ cm}^{-2})$	8.24 ^{+0.03} _{-0.07} (link)				
diskbb	T_{in} (keV)	1.02 ^{+0.10} _{-0.10}	1.16 ^{+0.02} _{-0.02}	1.41 ^{+0.03} _{-0.03}	1.14 ^{+0.03} _{-0.03}	1.31 ^{+0.02} _{-0.03}
	norm	214 ⁺¹¹⁰ ₋₆₂	431 ⁺³⁵ ₋₄₄	312 ⁺²⁸ ₋₂₄	547 ⁺⁴⁵ ₋₅₇	394 ⁺³⁴ ₋₃₀
	$R_{\text{in}} (R_{\text{g}})$	1.21 ^{+0.21} _{-0.18}	1.68 ^{+0.03} _{-0.03}	1.45 ^{+0.03} _{-0.03}	1.93 ^{+0.08} _{-0.07}	1.69 ^{+0.04} _{-0.04}
thcomp	τ_{hot}	2.93 ^{+0.27} _{-0.35}	1.84 ^{+0.07} _{-0.07}	1.67 ^{+0.12} _{-0.07}	1.80 ^{+0.15} _{-0.13}	1.51 ^{+0.09} _{-0.05}
	kT_{e}	20.7 ^{+2.8} _{-2.0}	29.5 ^{+1.4} _{-1.3}	28.1 ^{+2.8} _{-2.5}	28.2 ^{+3.6} _{-2.6}	31.9 ^{+2.4} _{-2.2}
	f_{sc}	0.76 ^{+0.09} _{-0.09}	1.00 ^{+P} _{-0.01}	1.00 ^{+P} _{-0.01}	1.0 ^{+P} _{-0.03}	1.0 ^{+P} _{-0.01}
$\chi^2/d.o.f$		572/671	1045/1097	1054/1085	887/1019	984/1046

Table 3. Simultaneous spectral fits using the model `constant * TBabs * thcomp * diskbb`. We first link all parameters together, and then untie one parameter at one time to check which parameter is critical to illustrate the spectral differences. see the text for details.

$\chi^2/d.o.f$.						
Parameter	All tied	T_{in} (keV)	norm	τ_{hot}	kT_{e} (keV)	f_{sc}
Epoch 1,2	30620/1759	1825/1758	1818/1757	1626/1756	1624/1755	1619/1754
Epoch 2,3	11200/2173	2623/2172	2622/2171	2102/2170	2102/2169	2102/2168
Parameter	All tied	norm	T_{in} (keV)	τ_{hot}	kT_{e} (keV)	f_{sc}
Epoch 1,2	30620/1759	1827/1758	1818/1757	1626/1756	1624/1755	1619/1754
Epoch 2,3	11200/2173	2676/2172	2622/2171	2102/2170	2102/2169	2102/2168
Parameter	All tied	τ_{hot}	kT_{e} (keV)	f_{sc}	T_{in} (keV)	norm
Epoch 1,2	30620/1759	4679/1758	4017/1757	3314/1756	1621/1755	1619/1754
Epoch 2,3	11200/2173	6742/2172	5143/2171	5143/2170	2118/2169	2102/2168
Parameter	All tied	kT_{e} (keV)	τ_{hot}	f_{sc}	T_{in} (keV)	norm
Epoch 1,2	30620/1759	5516/1758	4291/1757	4291/1756	1624/1755	1619/1754
Epoch 2,3	11200/2173	11122/2172	4726/2171	4726/2170	2118/2169	2102/2168
Parameter	All tied	f_{sc}	kT_{e} (keV)	τ_{hot}	T_{in} (keV)	norm
Epoch 1,2	30620/1759	3483/1758	3315/1757	3315/1756	1621/1755	1619/1754
Epoch 2,3	11200/2173	6142/2172	5570/2171	4619/2170	2118/2169	2102/2168

instead of the flare-like features shown in Figure 4. In particular, the PDS of the observation of the 1998 outburst show three extra prominent QPO features at ~ 4.7 Hz, ~ 7.0 Hz and ~ 13 Hz, in addition to the peak of the mHz QRM (Dieters et al. 2000; Trudolyubov et al. 2001). Further, Trudolyubov et al. (2001) investigated the flux-dependent properties of this observation. They divided the observation into two different flux levels and found that the ~ 13 Hz QPO is prominent at low fluxes, and disappears at high fluxes. The ~ 4.7 Hz QPO was

observed at low fluxes, and shifted to ~ 7 Hz at high fluxes. However, in the 2021 outburst, the type-C QPO is not simultaneously detected with the mHz QRM. We have also made a comparison of the PDS between the low-flux period and the high-flux period for our observations with the mHz QRM. No significant QPO signal was found in the 1–20 Hz range. To check the possibility of the presence of a low-frequency QPO, we add an extra Lorentzian component to the PDS with the frequency fixed at any potential peak in the frequency range

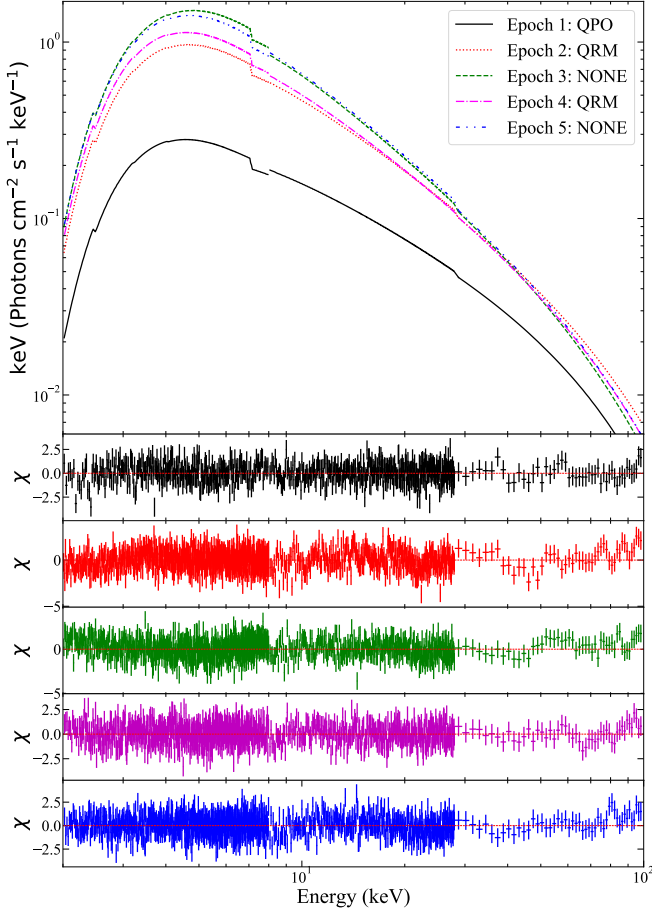


Figure 9. The best-fitting models and the corresponding residuals to the five spectra with model constant \ast TBabs \ast thcomp \ast diskbb.

1–10 Hz, and get a very low rms value ($< 1\%$). Therefore, we can rule out the presence of a significant low-frequency QPO when the mHz QRM appears.

Meanwhile, the appearance of mHz QRM is related to the accretion rate based on our results (see Figure 8), corresponding to $L_{2-100 \text{ keV}} \sim 0.16 L_{\text{Edd}}$ (assuming a distance of $D = 10 \text{ kpc}$). We have also checked the *RXTE* observations of the 1998 outburst and confirmed that the mHz QRM is also observed in a special flux plateau. Trudolyubov et al. (2001) suggested that the accretion-rate dependent flares might be common for black hole binaries emitting at a certain luminosity level. For 4U 1630–47, the appearance of the mHz QRM was observed at a very similar luminosity and position in HID compared to the 1998 outburst: the mHz QRM appears at a flux of $1.37 \times 10^{-8} \text{ erg s}^{-1} \text{ cm}^{-2}$ in 3–20 keV for 2021 outburst and at $1.40 \times 10^{-8} \text{ erg s}^{-1} \text{ cm}^{-2}$ for 1998 outburst. This behaviour can be explained by the local radiation dominated disk instability model, considering the occurrence of limit cycle behaviour under certain narrow accretion-rate range (Kato et al. 2008). Phenomenologically, the quasi-regular flare can be interpreted as the rapid removal

and replenishment of matter forming the inner region of the accretion disk, as observed in GRS 1915+105 (Belloni et al. 1997a). This process finishes a cycle on the viscous/thermal timescale.

Although the light curves of the mHz QRM seen in the 1998 and 2021 outbursts show different variations, the energy-dependent fractional rms and lag of the mHz QRM are similar (Zhao et al. in preparation). Considering that the mHz QRM appears in a similar flux range, we suggest that the mHz QRM seen in the two outbursts may have a similar physical origin.

Apart from the comparison with the 1998 outburst, we also compare this mHz QRM with the $\sim 11 \text{ mHz}$ QPO detected in H 1743–322 (Altamirano & Strohmayer 2012; Cheng et al. 2019). Altamirano & Strohmayer (2012) reported the detection of a $\sim 11 \text{ mHz}$ QPO in H 1743–322 at the beginning of the 2010 and 2011 outbursts. The mHz QPO was found at a similar spectral hardness value and intensity level, suggesting an accretion-rate dependence. We can see clear quasi-regular modulations from the light curves, similar to what we find in 4U 1630–47. However, the $\sim 11 \text{ mHz}$ QPO is much narrower ($Q \sim 10$) than the QRM observed in 4U 1630–47. In addition, the fractional rms amplitude of the $\sim 11 \text{ mHz}$ QPO is significantly lower ($3.1\% \pm 0.4\%$). Meanwhile, its energy-dependent properties also seems to be different from that found in 4U 1630–47 (Altamirano & Strohmayer 2012; Cheng et al. 2019). Therefore, it is not clear whether the two mHz signals have a similar physical origin or not.

4.2. Properties of the mHz QRM

Thanks for the large effective area and broad energy range of *Insight*-HXMT, we are able to investigate the energy dependence of the QRM properties to higher energy band. From Figure 5, we can see that both the fractional rms and characteristic frequency of the QRM increase with energy up to 60–100 keV. This positive correlation is more significant in fractional rms than in frequency, inferred from the results of linear function fitting. The energy-dependent fractional rms provides important evidence to constrain the physical origin of the mHz QRM. The increasing fractional rms up to 60–100 keV implies that the mHz QRM phenomenon is more pronounced for non-thermal components, the so-called corona/hot flow region. It is worth noticing that some sub-Eddington sources, such as IGR J17091–3624, also show this exotic variability while other Eddington-limited sources, such as GX 17+2 and V404 Cyg, do not (Court et al. 2017). Sądowski (2016) concluded that the disk size or minimum stabilizing large-scale magnetic field may be the unifying factor behind the objects that display GRS 1915-like variability. In conclusion, the results we obtained can well constrain the origin of the mHz QRM to the hot corona region.

The spectral evolution between different epochs provide more information on the physical origin of the transitions.

We find two transitions: from the epoch with the type-C QPO to the appearance of the mHz QRM, and from the epoch with the mHz QRM to the disappearance of the mHz QRM. The transition from the type-C QPO epoch to the mHz QPO epoch appears to be accompanied by an increase in inner disk radius. By comparing the optical depth of corona and scattering factor f_{sc} between epochs 1 and 2, we find that only $\sim 76\%$ of the seed photons are scattered in epoch 1, whereas nearly all photons from accretion disk are scattered in the Comptonization region in epoch 2. Meanwhile, the optical depth of the corona decreases from $\tau_{hot} = 2.93^{+0.27}_{-0.35}$ to $\tau_{hot} = 1.84^{+0.07}_{-0.07}$. Compared to the period without the mHz QRM, we find a colder inner disk and a larger disk radius when the mHz QRM appears in epoch 2 and 4. In addition to changes in diskbb parameters, we also find that, when the mHz QRM appears, the optical depth τ_{hot} is slightly higher. To summarize, the disk parameters and the optical depth have a significant effect on the goodness of the fits.

Meanwhile, the more or less zero lags below 10 keV and negative lags above 10 keV put strict restrictions on the origin of this mHz QRM. The magnitude of the time delays on timescales of seconds implies that they can not be produced by light travel time effects or Comptonization (Uttley et al. 2011). Considering the fast velocity of jet-like ejection ($v \sim 0.1c$), we cannot attribute the change of time delay to the change of the size of ejection. If it is the case, its size will be larger than 10,000 R_g . Mir et al. (2016) used the *RXTE*/PCA archival data of GRS 1915+015 during the " ρ " class, and produced the energy-dependent rms and time lag for the "heartbeat" modulation. They found that the time lags turn to a large soft lag at high energies, similar to what we found in 4U 1630–47 for the mHz QRM. However, the fractional rms turns around at ~ 10 keV, and then decreases to a lower value with energy. This is opposite to the positive correlation we observed in 4U 1630–47. Mir et al. (2016) proposed that there is a delayed response of the inner disk radius to the accretion rate. In this model, the fluctuating accretion rate in the outer disk drives the oscillations of the inner radius after a time delay up to several seconds, $r_{in}(t) \propto \dot{m}^\beta(t - \tau_d)$, while the power-law component responds immediately. They showed that, in such a scenario, a pure sinusoidal oscillation of the accretion rate can explain the shape and magnitude of the energy dependent rms and time lag of the "heartbeat" modulation seen in GRS 1915+015. However, in the case of 4U 1630–47, by broad band spectral analysis, we find that the spectra can be well-fitted by a single thermal Comptonization component ($f_{sc} = 1$) which fully scatters the seed photon from a multi-black body accretion disk. This means that the radiation from 1–100 keV is almost entirely from the Compton scattering of the corona. Meanwhile, the energy-dependent rms shown in Figure 5 cannot be fitted under the model that Mir et al. (2016)

presented. A further investigation on the model is needed in the future to explain the results shown in our work.

From epoch 1 to epoch 2, the decreasing optical depth suggests the expansion of the corona, leading to a decrease in electron density (Zdziarski et al. 2020). The expansion of the corona will also increase the coupled area between the disk and corona, thus leading to a fully scattered Comptonization spectrum and an increase in scattering fraction. We speculate that the joint region where the inner part of the accretion disk interacts with corona could be the place this flux modulation happens. An unknown instability with strict accretion rate dependence in the corona leads to the quasi-regular flux modulation. If the luminosity is slightly off the narrow luminosity range, the quasi-regular flux modulation will not appear to be accompanied with increasing disk temperature, which may reconstruct the coupling region between corona and accretion disk.

5. CONCLUSION

In this work, we present a detailed energy-dependent timing analysis and spectral comparison for the mHz QRM in 4U 1630–47. The main results are summarised as follows:

(1) The fractional rms of the mHz QRM increases with photon energy from 1 to 100 keV. The characteristic frequency of the mHz QRM increases marginally with energy. The phase/time lag of the mHz QRM is more or less zero below 10 keV and becomes negative above 10 keV. The absolute lag increases with energy from 10 keV up to 60–100 keV.

(2) The behaviour of the mHz QRM significantly depends on the accretion rate. The corresponding flux in 3–20 keV is about 1.37×10^{-8} erg s $^{-1}$ cm $^{-2}$, which is very close to that observed in the 1998 outburst.

(3) We measure the spectral differences among the periods with the type-C QPO, with the mHz QRM and without the mHz QRM. Compared with the type-C QPO spectra, the inner disk temperature increases, while the optical depth of the corona decreases when the mHz QRM appears. Meanwhile, the scattering fraction increases marginally from type-C epoch to mHz QRM epoch. Compared with the period without the mHz QRM, the optical depth of the corona is higher, while the inner disk temperature is slightly lower when the mHz QRM appears.

This mHz QRM phenomenon could be interpreted by an unknown instability in corona that causes the flux modulation. Meanwhile, the change of corona optical depth/size and inner temperature of disk may be related to the appearance of the mHz QRM. However, a more complex model is needed to explain the energy-dependence rms and time lag. Observations of the mHz QRM with future X-ray telescopes, e.g., the enhanced X-ray Timing and Polarimetry mission (eXTP, Zhang et al. 2019), are required to perform a more detailed

time/phase-resolved analysis and give a deeper insight into its physical origin.

We are grateful for the anonymous referee's helpful comments and suggestions. This work has made use of the data from the *Insight*-HXMT mission, a project funded by China National Space Administration (CNSA) and the Chinese Academy of Sciences (CAS), and data and/or software provided by the High Energy Astrophysics Science Archive Research Center (HEASARC), a service of the Astrophysics Science Division at NASA/GSFC. This work is supported by the National Key RD Program of China (2021YFA0718500) and the National Natural Science Foundation of China (NSFC) under grants U1838201, U1838202, 11733009, 11673023,

U1938102, U2038104, U2031205, the CAS Pioneer Hundred Talent Program (grant No. Y8291130K2) and the Scientific and Technological innovation project of IHEP (grant No. Y7515570U1).

Software: XSPEC (Arnaud 1996), Astropy (Astropy Collaboration et al. 2013), Numpy (van der Walt et al. 2011), Matplotlib (Hunter 2007), Stingray (Huppenkothen et al. 2019a,b).

DATA AVAILABILITY

The raw data underlying this article are available at <http://hxmtcn.ihep.ac.cn/>.

REFERENCES

- Abe, Y., Fukazawa, Y., Kubota, A., Kasama, D., & Makishima, K. 2005, PASJ, 57, 629, doi: [10.1093/pasj/57.4.629](https://doi.org/10.1093/pasj/57.4.629)
- Altamirano, D., & Strohmayer, T. 2012, ApJL, 754, L23, doi: [10.1088/2041-8205/754/2/L23](https://doi.org/10.1088/2041-8205/754/2/L23)
- Altamirano, D., Belloni, T., Linares, M., et al. 2011, ApJL, 742, L17, doi: [10.1088/2041-8205/742/2/L17](https://doi.org/10.1088/2041-8205/742/2/L17)
- Arnaud, K. A. 1996, in Astronomical Society of the Pacific Conference Series, Vol. 101, Astronomical Data Analysis Software and Systems V, ed. G. H. Jacoby & J. Barnes, 17
- Astropy Collaboration, Robitaille, T. P., Tollerud, E. J., et al. 2013, A&A, 558, A33, doi: [10.1051/0004-6361/201322068](https://doi.org/10.1051/0004-6361/201322068)
- Baby, B. E., Agrawal, V. K., Ramadevi, M. C., et al. 2020, MNRAS, 497, 1197, doi: [10.1093/mnras/staa1965](https://doi.org/10.1093/mnras/staa1965)
- Belloni, T., & Hasinger, G. 1990, A&A, 227, L33
- Belloni, T., Klein-Wolt, M., Méndez, M., van der Klis, M., & Paradijs, J. 2000, A&A, 355, 271, <https://arxiv.org/abs/astro-ph/0001103>
- Belloni, T., Méndez, M., King, A. R., van der Klis, M., & Paradijs, J. 1997a, ApJL, 479, L145, doi: [10.1086/310595](https://doi.org/10.1086/310595)
- Belloni, T., Psaltis, D., & van der Klis, M. 2002, ApJ, 572, 392, doi: [10.1086/340290](https://doi.org/10.1086/340290)
- Belloni, T., van der Klis, M., Lewin, W. H. G., et al. 1997b, A&A, 322, 857
- Belloni, T. M., & Stella, L. 2014, SSRv, 183, 43, doi: [10.1007/s11214-014-0076-0](https://doi.org/10.1007/s11214-014-0076-0)
- Bu, Q.-c., Chen, L., Li, Z.-s., et al. 2015, ApJ, 799, 2, doi: [10.1088/0004-637X/799/1/2](https://doi.org/10.1088/0004-637X/799/1/2)
- Bu, Q. C., Zhang, S. N., Santangelo, A., et al. 2021, ApJ, 919, 92, doi: [10.3847/1538-4357/ac11f5](https://doi.org/10.3847/1538-4357/ac11f5)
- Cao, X., Jiang, W., Meng, B., et al. 2020, SCPMA, 63, 249504, doi: [10.1007/s11433-019-1506-1](https://doi.org/10.1007/s11433-019-1506-1)
- Capitanio, F., Campana, R., De Cesare, G., & Ferrigno, C. 2015, MNRAS, 450, 3840, doi: [10.1093/mnras/stv687](https://doi.org/10.1093/mnras/stv687)
- Casella, P., Belloni, T., & Stella, L. 2005, ApJ, 629, 403, doi: [10.1086/431174](https://doi.org/10.1086/431174)
- Chen, Y., Cui, W., Li, W., et al. 2020, SCPMA, 63, 249505, doi: [10.1007/s11433-019-1469-5](https://doi.org/10.1007/s11433-019-1469-5)
- Chen, Y. P., Zhang, S., Qu, J. L., et al. 2018, ApJL, 864, L30, doi: [10.3847/2041-8213/aadc0e](https://doi.org/10.3847/2041-8213/aadc0e)
- Cheng, Z., Méndez, M., Altamirano, D., Beri, A., & Wang, Y. 2019, MNRAS, 482, 550, doi: [10.1093/mnras/sty2695](https://doi.org/10.1093/mnras/sty2695)
- Choudhury, M., Bhatt, N., & Bhattacharyya, S. 2015, MNRAS, 447, 3960, doi: [10.1093/mnras/stu2742](https://doi.org/10.1093/mnras/stu2742)
- Connors, R. M. T., García, J. A., Tomsick, J., et al. 2021, ApJ, 909, 146, doi: [10.3847/1538-4357/abdd2c](https://doi.org/10.3847/1538-4357/abdd2c)
- Court, J. M. C., Altamirano, D., Pereyra, M., et al. 2017, MNRAS, 468, 4748, doi: [10.1093/mnras/stx773](https://doi.org/10.1093/mnras/stx773)
- Dieters, S. W., Belloni, T., Kuulkers, E., et al. 2000, ApJ, 538, 307, doi: [10.1086/309108](https://doi.org/10.1086/309108)
- Done, C., Gierliński, M., & Kubota, A. 2007, A&A Rv, 15, 1, doi: [10.1007/s00159-007-0006-1](https://doi.org/10.1007/s00159-007-0006-1)
- Dzielałak, M. A., De Marco, B., & Zdziarski, A. A. 2021, MNRAS, 506, 2020, doi: [10.1093/mnras/stab1700](https://doi.org/10.1093/mnras/stab1700)
- Feng, M. Z., Kong, L. D., Wang, P. J., et al. 2022, arXiv e-prints, arXiv:2201.08588. <https://arxiv.org/abs/2201.08588>
- Guo, C.-C., Liao, J.-Y., Zhang, S., et al. 2020, Journal of High Energy Astrophysics, 27, 44, doi: [10.1016/j.jheap.2020.02.008](https://doi.org/10.1016/j.jheap.2020.02.008)
- Hannikainen, D. C., Rodriguez, J., Vilhu, O., et al. 2005, A&A, 435, 995, doi: [10.1051/0004-6361:20042250](https://doi.org/10.1051/0004-6361:20042250)
- Huang, Y., Qu, J. L., Zhang, S. N., et al. 2018, ApJ, 866, 122, doi: [10.3847/1538-4357/aade4c](https://doi.org/10.3847/1538-4357/aade4c)
- Hunter, J. D. 2007, Computing in Science and Engineering, 9, 90, doi: [10.1109/MCSE.2007.55](https://doi.org/10.1109/MCSE.2007.55)
- Huppenkothen, D., Bachetti, M., Stevens, A. L., et al. 2019a, ApJ, 881, 39, doi: [10.3847/1538-4357/ab258d](https://doi.org/10.3847/1538-4357/ab258d)

- Huppenkothen, D., Bachetti, M., Stevens, A., et al. 2019b, *The Journal of Open Source Software*, 4, 1393, doi: [10.21105/joss.01393](https://doi.org/10.21105/joss.01393)
- Ingram, A., & Done, C. 2010, *MNRAS*, 405, 2447, doi: [10.1111/j.1365-2966.2010.16614.x](https://doi.org/10.1111/j.1365-2966.2010.16614.x)
- . 2011, *MNRAS*, 415, 2323, doi: [10.1111/j.1365-2966.2011.18860.x](https://doi.org/10.1111/j.1365-2966.2011.18860.x)
- Ingram, A., Done, C., & Fragile, P. C. 2009, *MNRAS*, 397, L101, doi: [10.1111/j.1745-3933.2009.00693.x](https://doi.org/10.1111/j.1745-3933.2009.00693.x)
- Ingram, A. R., & Motta, S. E. 2019, *NewAR*, 85, 101524, doi: [10.1016/j.newar.2020.101524](https://doi.org/10.1016/j.newar.2020.101524)
- Jones, C., Forman, W., Tananbaum, H., & Turner, M. J. L. 1976, *ApJL*, 210, L9, doi: [10.1086/182291](https://doi.org/10.1086/182291)
- Kalamkar, M., Casella, P., Uttley, P., et al. 2016, *MNRAS*, 460, 3284, doi: [10.1093/mnras/stw1211](https://doi.org/10.1093/mnras/stw1211)
- Kalemci, E., Maccarone, T. J., & Tomsick, J. A. 2018, *ApJ*, 859, 88, doi: [10.3847/1538-4357/aabcd3](https://doi.org/10.3847/1538-4357/aabcd3)
- Kato, S., Fukue, J., & Mineshige, S. 2008, *Black-Hole Accretion Disks — Towards a New Paradigm —*
- King, A. L., Walton, D. J., Miller, J. M., et al. 2014, *ApJL*, 784, L2, doi: [10.1088/2041-8205/784/1/L2](https://doi.org/10.1088/2041-8205/784/1/L2)
- Klein-Wolt, M., Fender, R. P., Pooley, G. G., et al. 2002, *MNRAS*, 331, 745, doi: [10.1046/j.1365-8711.2002.05223.x](https://doi.org/10.1046/j.1365-8711.2002.05223.x)
- Kuulkers, E., Parmar, A. N., Kitamoto, S., Cominsky, L. R., & Sood, R. K. 1997, *MNRAS*, 291, 81, doi: [10.1093/mnras/291.1.81](https://doi.org/10.1093/mnras/291.1.81)
- Liao, J.-Y., Zhang, S., Lu, X.-F., et al. 2020a, *Journal of High Energy Astrophysics*, 27, 14, doi: [10.1016/j.jheap.2020.04.002](https://doi.org/10.1016/j.jheap.2020.04.002)
- Liao, J.-Y., Zhang, S., Chen, Y., et al. 2020b, *Journal of High Energy Astrophysics*, 27, 24, doi: [10.1016/j.jheap.2020.02.010](https://doi.org/10.1016/j.jheap.2020.02.010)
- Lightman, A. P., & Eardley, D. M. 1974, *ApJL*, 187, L1, doi: [10.1086/181377](https://doi.org/10.1086/181377)
- Liu, C., Zhang, Y., Li, X., et al. 2020, *SCPMA*, 63, 249503, doi: [10.1007/s11433-019-1486-x](https://doi.org/10.1007/s11433-019-1486-x)
- Liu, Q., Liu, H., Bambi, C., & Ji, L. 2021, *arXiv e-prints*, arXiv:2111.00719. <https://arxiv.org/abs/2111.00719>
- Ma, X., Tao, L., Zhang, S.-N., et al. 2021, *Nature Astronomy*, 5, 94, doi: [10.1038/s41550-020-1192-2](https://doi.org/10.1038/s41550-020-1192-2)
- Méndez, M., Karpouzas, K., García, F., et al. 2022, *Nature Astronomy*, 6, 577, doi: [10.1038/s41550-022-01617-y](https://doi.org/10.1038/s41550-022-01617-y)
- Mineo, T., Massa, F., Massaro, E., & Feroci, M. 2021, *A&A*, 650, A122, doi: [10.1051/0004-6361/202040251](https://doi.org/10.1051/0004-6361/202040251)
- Mir, M. H., Misra, R., Pahari, M., Iqbal, N., & Ahmad, N. 2016, *MNRAS*, 457, 2999, doi: [10.1093/mnras/stw156](https://doi.org/10.1093/mnras/stw156)
- Miyamoto, S., Kimura, K., Kitamoto, S., Dotani, T., & Ebisawa, K. 1991, *ApJ*, 383, 784, doi: [10.1086/170837](https://doi.org/10.1086/170837)
- Morgan, E. H., Remillard, R. A., & Greiner, J. 1997, *ApJ*, 482, 993, doi: [10.1086/304191](https://doi.org/10.1086/304191)
- Motta, S., Muñoz-Darias, T., Casella, P., Belloni, T., & Homan, J. 2011, *MNRAS*, 418, 2292, doi: [10.1111/j.1365-2966.2011.19566.x](https://doi.org/10.1111/j.1365-2966.2011.19566.x)
- Neilsen, J., Remillard, R. A., & Lee, J. C. 2012, *ApJ*, 750, 71, doi: [10.1088/0004-637X/750/1/71](https://doi.org/10.1088/0004-637X/750/1/71)
- Pahari, M., Bhattacharyya, S., Rao, A. R., et al. 2018, *ApJ*, 867, 86, doi: [10.3847/1538-4357/aae53b](https://doi.org/10.3847/1538-4357/aae53b)
- Parmar, A. N., Angelini, L., & White, N. E. 1995, *ApJL*, 452, L129, doi: [10.1086/309730](https://doi.org/10.1086/309730)
- Priedhorsky, W. 1986, *Ap&SS*, 126, 89, doi: [10.1007/BF00644177](https://doi.org/10.1007/BF00644177)
- Qu, J. L., Lu, F. J., Lu, Y., et al. 2010, *ApJ*, 710, 836, doi: [10.1088/0004-637X/710/1/836](https://doi.org/10.1088/0004-637X/710/1/836)
- Rawat, D., Misra, R., Jain, P., & Yadav, J. S. 2022, *MNRAS*, 511, 1841, doi: [10.1093/mnras/stac154](https://doi.org/10.1093/mnras/stac154)
- Remillard, R. A., Morgan, E. H., McClintock, J. E., Bailyn, C. D., & Orosz, J. A. 1999, *ApJ*, 522, 397, doi: [10.1086/307606](https://doi.org/10.1086/307606)
- Seifina, E., Titarchuk, L., & Shaposhnikov, N. 2014, *ApJ*, 789, 57, doi: [10.1088/0004-637X/789/1/57](https://doi.org/10.1088/0004-637X/789/1/57)
- Sądowski, A. 2016, *MNRAS*, 462, 960, doi: [10.1093/mnras/stw1852](https://doi.org/10.1093/mnras/stw1852)
- Soleri, P., Belloni, T., & Casella, P. 2008, *MNRAS*, 383, 1089, doi: [10.1111/j.1365-2966.2007.12596.x](https://doi.org/10.1111/j.1365-2966.2007.12596.x)
- Sriram, K., Rao, A. R., & Choi, C. S. 2013, *ApJ*, 775, 28, doi: [10.1088/0004-637X/775/1/28](https://doi.org/10.1088/0004-637X/775/1/28)
- Tomsick, J. A., Corbel, S., Goldwurm, A., & Kaaret, P. 2005, *ApJ*, 630, 413, doi: [10.1086/431896](https://doi.org/10.1086/431896)
- Tomsick, J. A., Lapshov, I., & Kaaret, P. 1998, *ApJ*, 494, 747, doi: [10.1086/305240](https://doi.org/10.1086/305240)
- Tomsick, J. A., Yamaoka, K., Corbel, S., et al. 2014, *ApJ*, 791, 70, doi: [10.1088/0004-637X/791/1/70](https://doi.org/10.1088/0004-637X/791/1/70)
- Trudolyubov, S. P., Borozdin, K. N., & Priedhorsky, W. C. 2001, *MNRAS*, 322, 309, doi: [10.1046/j.1365-8711.2001.04073.x](https://doi.org/10.1046/j.1365-8711.2001.04073.x)
- Uttley, P., Wilkinson, T., Cassatella, P., et al. 2011, *MNRAS*, 414, L60, doi: [10.1111/j.1745-3933.2011.01056.x](https://doi.org/10.1111/j.1745-3933.2011.01056.x)
- van der Klis, M. 2006, in *Compact stellar X-ray sources*, Vol. 39, 39–112
- van der Walt, S., Colbert, S. C., & Varoquaux, G. 2011, *Computing in Science and Engineering*, 13, 22, doi: [10.1109/MCSE.2011.37](https://doi.org/10.1109/MCSE.2011.37)
- Vaughan, B. A., & Nowak, M. A. 1997, *ApJL*, 474, L43, doi: [10.1086/310430](https://doi.org/10.1086/310430)
- Wang, P. J., Kong, L. D., Chen, Y. P., et al. 2022, *MNRAS*, 512, 4541, doi: [10.1093/mnras/stac773](https://doi.org/10.1093/mnras/stac773)
- Weng, S.-S., Wang, T.-T., Cai, J.-P., Yuan, Q.-R., & Gu, W.-M. 2018, *ApJ*, 865, 19, doi: [10.3847/1538-4357/aad9a6](https://doi.org/10.3847/1538-4357/aad9a6)
- Yang, Z.-X., Zhang, L., Bu, Q.-C., et al. 2022, *ApJ*, 932, 7, doi: [10.3847/1538-4357/ac63af](https://doi.org/10.3847/1538-4357/ac63af)
- Zdziarski, A. A., Johnson, W. N., & Magdziarz, P. 1996, *MNRAS*, 283, 193, doi: [10.1093/mnras/283.1.193](https://doi.org/10.1093/mnras/283.1.193)

- Zdziarski, A. A., Szanecki, M., Poutanen, J., Gierliński, M., & Biernacki, P. 2020, *MNRAS*, 492, 5234, doi: [10.1093/mnras/staa159](https://doi.org/10.1093/mnras/staa159)
- Zhang, L., Wang, Y., Méndez, M., et al. 2017, *ApJ*, 845, 143, doi: [10.3847/1538-4357/aa8138](https://doi.org/10.3847/1538-4357/aa8138)
- Zhang, L., Altamirano, D., Uttley, P., et al. 2021, *MNRAS*, 505, 3823, doi: [10.1093/mnras/stab1553](https://doi.org/10.1093/mnras/stab1553)
- Zhang, S., Santangelo, A., Feroci, M., et al. 2019, *Science China Physics, Mechanics, and Astronomy*, 62, 29502, doi: [10.1007/s11433-018-9309-2](https://doi.org/10.1007/s11433-018-9309-2)
- Zhang, S.-N., Li, T., Lu, F., et al. 2020, *SCPMA*, 63, 249502, doi: [10.1007/s11433-019-1432-6](https://doi.org/10.1007/s11433-019-1432-6)
- Zhang, Z., Qu, J. L., Gao, H. Q., et al. 2014, *A&A*, 569, A33, doi: [10.1051/0004-6361/201323294](https://doi.org/10.1051/0004-6361/201323294)
- Zhang, Z., Qu, J. L., Gao, H. Q., & Zhou, J. N. 2013, in *Feeding Compact Objects: Accretion on All Scales*, ed. C. M. Zhang, T. Belloni, M. Méndez, & S. N. Zhang, Vol. 290, 364–366, doi: [10.1017/S174392131202042X](https://doi.org/10.1017/S174392131202042X)